Research Article | Open Access

Soft Science

Ding *et al. Soft Sci.* **2026**, *6*, 2 **DOI:**10.20517/ss.2025.113

Hollow $Zn_{1-x}Co_{2-y}Ni_xFe_yO_4$ spinel via multi-metal ion doping: ultralight and broadband microwave absorber

Lianfei Ding, Zizhuang He, Ruina Zhang, Sihan Liu, Wangchang Geng*, Panbo Liu*

Keywords:
Hollow structure, ion doping, spinel, MOFs, electromagnetic wave absorption

Citation: Ding, L.; He, Z.; Zhang, R.; Liu, S.; Geng, W.; Liu, P. Hollow $Zn_{1-x}Co_{2-y}Ni_xFe_yO_4$ spinel via multi-metal ion doping: ultralight and broadband microwave absorber. *Soft Sci.* **2026**, *6*, 2. https://dx.doi.org/10.20517/ss.2025.113

Received: 1 Nov 2025
First Decision: 21 Nov 2025
Revised: 5 Dec 2025
Accepted: 16 Dec 2025
Published: 14 Jan 2026

Academic Editors:
Hu Liu, YongAn Huang
Copy Editor:
Xing-Yue Zhang
Production Editor:
Xing-Yue Zhang

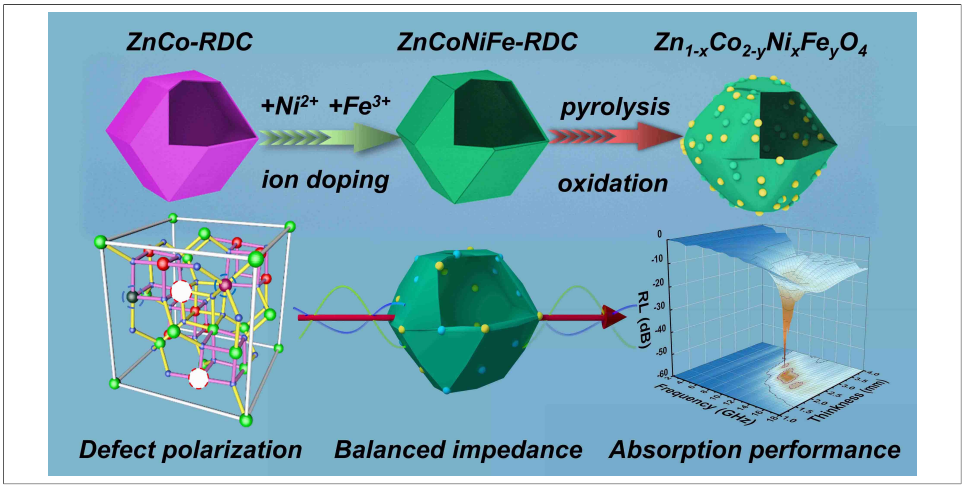

Abstract

Hollow architectures offer significant advantages in achieving simultaneous weight reduction and efficient electromagnetic (EM) wave absorption; however, their practical application is often constrained by inherent structural limitations. In this study, $Zn_{1-x}Co_{2-y}Ni_xFe_yO_4$ composites were synthesized through an integrated self-sacrificing templating and ion-doping approach. Specifically, mixed zeolitic imidazolate frameworks (ZIFs) were utilized as sacrificial templates to fabricate hollow dodecahedral nanocages. Subsequent ion doping was facilitated by the chelating effect of tannic acid, followed by oxidative annealing in a tube furnace. Interestingly, the introduction of hetero-metal ions disturbed the original spinel lattice structure, leading to the extensive precipitation of a secondary ZnO phase. This spontaneous phase separation generated a high density of heterogeneous interfaces, which significantly enhanced interfacial polarization and thereby improved overall EM wave attenuation performance. These structural and compositional features enable the material to exhibit excellent microwave absorption capabilities even at low filler loadings. The hollow architecture not only reduces the intrinsic density of spinel ferrites but also extends the effective absorption bandwidth by optimizing impedance matching characteristics. As a result, a minimum reflection loss of -57.6 dB and an effective absorption bandwidth of 10.27 GHz were achieved with a filler content as low as 30 wt.%.

School of Chemistry and Chemical Engineering, Northwestern Polytechnical University, Xi'an 710129, Shaanxi, China.

***Correspondence to:** Prof. Wangchang Geng, Prof. Panbo Liu, School of Chemistry and Chemical Engineering, Northwestern Polytechnical University, Xi'an 710129, Shaanxi, China. E-mail: w.geng@nwpu.edu.cn; liupanbo@nwpu.edu.cn

This work presents a new strategy for the rational design of high-performance EM absorbers through the synergistic optimization of structural architecture and compositional modulation.

INTRODUCTION

Driven by advancements in wireless communication - most notably the large-scale deployment of 5G networks and Internet of Things (IoT) technologies - a growing diversity of smart devices has emerged, significantly enhancing daily convenience[1-6]. However, the intrinsic electromagnetic (EM) emissions of these systems give rise to EM pollution, which can undermine the operational integrity of precision instruments and impose non-negligible risks to human health. Accordingly, the rational design of EM metasurfaces and the microscale engineering of the effective attenuation properties of EM-absorbing materials are widely acknowledged as effective strategies for mitigating such pollution[7-10]. It is worth noting that the fabrication of metasurfaces typically depends on emerging technologies such as three-dimensional printing and machine learning, making their areal cost per square foot prohibitive for large-scale implementation. Consequently, the microscale modulation of the EM dissipation characteristics of composite powders has become the dominant approach for developing next-generation microwave-absorbing materials[11-14]. Unfortunately, most existing particulate systems are now approaching the theoretical limit defined by the Rozanov bound, thus failing to meet the stringent bandwidth requirements of contemporary applications[15].

In recent years, metal-organic frameworks (MOFs) and their derivatives have been the subject of extensive investigation as EM wave-absorbing media, courtesy of their precisely tunable chemical compositions, hierarchically porous architectures, and diverse micro-morphologies[16-19]. Specifically, mixed-metal oxides derived from polymetallic MOFs allow atom-level engineering of crystal structures through deliberate selection and stoichiometric adjustment of constituent metal ions, thereby enabling straightforward control over dielectric parameters. Notably, the ultra-dense atomic packing inherent to the spinel lattice confers a significantly reduced formation energy during low-temperature oxidative pyrolysis of polymetallic MOFs under ambient air conditions. This makes the spinel phase a thermodynamically favorable and structurally robust matrix for EM absorption[20]. However, akin to conventional ferrite-type absorbers, the high mass fraction typically required to achieve sufficient attenuation has long posed a barrier to practical implementation. Furthermore, oxide ceramics typically exhibit moderate dielectric constants and limited dielectric loss, which constrains their ability to achieve strong and broadband absorption within targeted spectral windows[21]. To bypass the Snock limit and achieve pronounced EM dissipation in the mid-to-high gigahertz range, growing attention has been devoted to the construction of spinel/carbon heterostructures[22,23]. Within these architectures, the unavoidable cation/anion site disorder intrinsic to the spinel lattice, together with high-density dislocations, grain boundaries, and sub-grain boundaries generated during pyrolysis, provides abundant polarization and relaxation centers. These centers can be strategically leveraged to modulate EM attenuation[24]. Correspondingly, indirectly tuning the dielectric and magnetic properties of spinel-based absorbers through low-temperature pyrolysis of MOFs with tailored metal nodes constitutes an effective approach to reducing the minimum reflection loss (RLmin). Post-synthetic etching and ion-exchange protocols that induce spinel frameworks incorporating mesoporous and macroporous hierarchies further serve as powerful tools for impedance engineering[25,26]. While extensive research efforts have focused on reducing the mass loading of spinel-based absorbers to enhance impedance matching, the synergistic effect of ionic doping and microstructural design on EM performance remains largely underexplored.

Herein, a systematic strategy combining architectural engineering with compositional regulation was developed to synthesize the $Zn_{1-x}Co_{2-y}Ni_xFe_yO_4$ composite. Hollow rhombic dodecahedral cages (ZnCo-RDC) were fabricated using bimetallic MOF ZnCo-zeolitic imidazolate frameworks (ZIFs) as the sacrificial template and tannic acid (TA) as the etchant. TA played dual core roles in this process. First, it enabled

conformal etching through its weak acidity and coordination protection effect, gradually hollowing the interior while preserving the intact rhombic dodecahedral morphology, thus constructing a well-defined hollow structure. Second, the abundant phenolic hydroxyl groups in TA molecules formed strong chelation with metal ions, providing active sites for the subsequent uniform doping of Fe^{3+} and Ni^{2+}. Based on this etching-chelation synergistic mechanism, TA, Fe^{3+} and Ni^{2+} were quantitatively incorporated into the material framework, achieving precise modulation of the EM transmission properties. Following calcination at 550 °C in ambient air, a phase-pure spinel structure was obtained. At a filler loading of 30 wt.%, the optimally modified $Zn_{1-x}Co_{2-y}Ni_xFe_yO_4$ composite achieves a RLmin of -57.6 dB, with a corresponding effective absorption bandwidth (EAB) as wide as 10.27 GHz. Notably, this bandwidth range fully covers the entire X-band (8~12 GHz) and Ku-band (12~18 GHz). These enhanced microwave absorption properties are attributed to the synergistic effects of the hollow architecture, abundant heterointerfaces, and multi-cation doping. This study not only proposes a simple and scalable method for addressing the intrinsic bandwidth limitations of powder-based absorbers but also highlights the pivotal role of microscale ionic substitution in tuning EM transport behavior. The findings contribute to bridging the gap between microscopic property control and macroscopic device integration, while the facile synthesis approach offers a viable route for the practical application of microwave-absorbing materials in real-world far-field scenarios.

EXPERIMENTAL

Materials

Zinc nitrate hexahydrate [$Zn(NO_3)_2·6H_2O$], methanol, and nickel chloride hexahydrate ($NiCl_2·6H_2O$) were purchased from Guangdong Guanghua Technology Co., Ltd. (Guangdong, China); ferric chloride hexahydrate ($FeCl_3·6H_2O$) and cobalt nitrate hexahydrate [$Co(NO_3)_2·6H_2O$] were purchased from Shanghai McLean Biochemical Technology Co., Ltd. (Shanghai, China); TA and 2-methylimidazole (2-Melm) were purchased from Shanghai Aladdin Biochemical Technology Co., Ltd. (Shanghai, China).

Preparation of ZnCo-ZIFs

A total of 1.15 g of $Co(NO_3)_2·6H_2O$ and 1.18 g of $Zn(NO_3)_2·6H_2O$ were co-dissolved in 50 mL of methanol. This metal salt solution was then slowly added dropwise to 50 mL of a methanol solution containing 2.87 g of 2-Melm, and the reaction mixture was continuously stirred at room temperature for 40 min. After allowing the reaction system to stand undisturbed for 24 h, the product was collected by centrifugation, washed thoroughly with ethanol multiple times to remove residual impurities, and finally dried to yield the ZnCo-ZIFs.

Preparation of ZnCo-RDC

A total of 20 mg of the as-synthesized ZnCo-ZIFs was accurately weighed and dispersed in 10 mL of ethanol. The resulting dispersion was then carefully added to 100 mL of a 1 mg/mL TA solution, in which the solvent was a 1:1 (v/v) ethanol-water mixture. After stirring the mixture at room temperature for 10 min, unreacted TA was removed by washing with ethanol. Following drying, ZnCo-RDC was successfully obtained.

Preparation of ZnCoFeNi-RDC

For the ion doping experiment, 5.4 mg of $FeCl_3·6H_2O$ and 4.7 mg of $NiCl_2·6H_2O$ were dissolved in 40 mL of deionized water. The solution was vigorously stirred to ensure the formation of a homogeneous metal ion mixture. This mixture was then slowly added dropwise into 60 mL of a 1 mg/mL TA-ZnCo ethanol dispersion, and the reaction mixture was continuously stirred for 3 h. After completion of the reaction, the product was washed multiple times with ethanol and then dried, yielding the iron-nickel double ion-doped precursor (ZnCoFeNi-RDC). When using only a single metal salt for doping, the corresponding single metal-doped precursors, such as ZnCoFe-RDC or ZnCoNi-RDC, can be synthesized following a similar procedure.

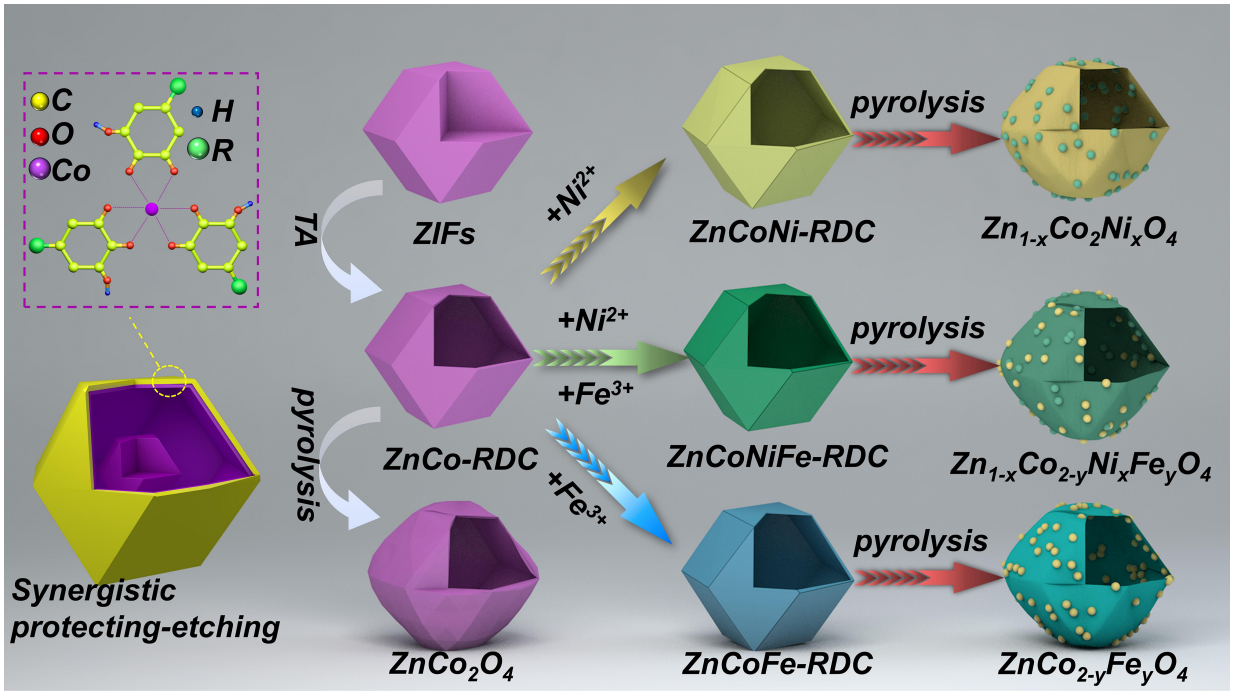

Figure 1. Synthetic procedure for the preparation of $Zn_{1-x}Co_{2-y}Ni_xFe_yO_4$ nanomaterials. Created using Cinema 4D R20. TA: Tannic acid; ZIFs: zeolitic imidazolate frameworks; RDC: rhombic dodecahedral cage.

Preparation of $Zn_{1-x}Co_{2-y}Ni_xFe_yO_4$

The as-prepared ZnCoFeNi-RDC precursor was loaded into a tube furnace and subjected to annealing treatment in an oxygen atmosphere. The heating protocol was meticulously designed as follows: the temperature was ramped up to 200 °C at a controlled rate of 2 °C/min and held at this temperature for 1 h; it was then further increased to 550 °C at the same rate and maintained for 2 h. Upon completion of the annealing process, the sample was allowed to cool spontaneously to room temperature, ultimately yielding $Zn_{1-x}Co_{2-y}Ni_xFe_yO_4$. Figure 1 illustrates the synthesis process of $Zn_{1-x}Co_2Ni_xFe_yO_4$.

RESULTS AND DISCUSSION

Scanning electron microscopy (SEM) and transmission electron microscopy (TEM) images of the corresponding precursors are presented in Supplementary Figures 1-8, demonstrating that ZnCo-ZIFs evolved into hollow and structurally stable dodecahedral nanocages following TA etching (detailed parameters of the characterization instruments are provided in the Supplementary Materials). Furthermore, the overall morphology remained largely unchanged during the subsequent annealing process, as evidenced by the representative micrographs in Figure 2A-D. High-resolution SEM images [Figure 2E-H] further reveal that the annealed material exhibits a multiphase coexistence state, with nanoparticles precipitated on the matrix surface. TEM characterization [Figure 2I] verified that the sample maintained a well-preserved hollow framework. Notably, subsequent to the doping treatment, new nanoparticles were observed on the inner surface of the shell cavity [Figure 2J-L]. Figure 2M displays a high-resolution TEM (HRTEM) micrograph where the lattice fringes of $ZnCo_2O_4$ nanocrystals are distinctly resolved. Fast-Fourier-transform (FFT) indexing confirms an interplanar spacing of 0.246 nm, which matches the d-spacing of the (311) plane in spinel-structured $ZnCo_2O_4$. Comparative HRTEM analyses of $Zn_{1-x}Co_2Ni_xO_4$, $ZnCo_{2-y}Fe_yO_4$ and $Zn_{1-x}Co_{2-y}Ni_xFe_yO_4$ [Figure 2N-P, Supplementary Figure 9] reveal a systematic lattice contraction: the (311) interplanar spacing decreases from 0.246 to 0.224, 0.226 and 0.224 nm, respectively. This contraction arises from the substitution of smaller Fe^{3+} and Ni^{2+} cations for larger Co^{3+} and Zn^{2+} ions. In addition, lattice fringes with spacings of 0.250, 0.252, and 0.247 nm were observed, respectively, corresponding to the (101) crystal plane of hexagonal zinc oxide. This observation confirms the precipitation of the secondary zinc oxide phase

during the doping process. This observation confirms the exsolution of a secondary ZnO phase during the doping process. High-resolution energy-dispersive X-ray spectroscopic (EDS) elemental mapping further clarifies the spatial distribution of Zn, Co, O, and the dopant metals (Ni/Fe). Post-doping, localized enrichment of Zn and O leads to the formation of discrete crystallites that form coherent, atomically sharp interfaces with the $ZnCo_2O_4$ matrix. These atomically abrupt hetero-interfaces generate abundant interfacial polarization centers, which are expected to significantly enhance EM wave attenuation[27].

To achieve optimal crystallinity while suppressing excessive grain growth, an annealing temperature of 550 °C was chosen [Figure 3A]. X-ray diffraction (XRD) patterns [Figure 3B] reveal that a trace amount of ZnO phase is detectable in the as-prepared $ZnCo_2O_4$. This is attributed to the 1:1 Zn/Co stoichiometric ratio of the ZIF precursors, leading to the enrichment of Zn^{2+} in the lattice and the subsequent precipitation of ZnO during the annealing process. Upon the incorporation of foreign metal ions, most spinel-related diffraction reflections are significantly attenuated, whereas the diffraction peaks corresponding to ZnO become dominant[28]. This evolutionary trend indicates that aliovalent doping promotes further exsolution of the ZnO phase. The underlying mechanism involves dopant-induced lattice distortion, which destabilizes the parent spinel framework, reduces the associated lattice energy, and thereby drives the segregation of ZnO from the host lattice. Meanwhile, the XRD patterns of the precursor and its corresponding annealed product are provided in Supplementary Figure 10. Raman spectroscopy [Figure 3C] was used to investigate the vibrational characteristics of the four specimens. In line with its spinel symmetry, pristine $ZnCo_2O_4$ displays two distinct Raman-active modes at approximately 470 cm^{-1} (Eg) and 680 cm^{-1} (A_1g)[29]. The A_1g mode originates from the symmetric O-Co^{3+}-O stretching vibration within octahedral units and is highly sensitive to the ordering degree of Co^{3+} ions[30]. In contrast, the doubly degenerate Eg mode corresponds to the cooperative bending motion involving both Co^{3+} and Zn^{2+} cations, thus functioning as a probe for the overall lattice symmetry. Upon Fe^{3+} substitution, the intensity of the A_1g band undergoes significant attenuation and is completely eliminated after dual-metal doping. Concomitantly, the Eg mode gradually weakens and eventually disappears. These systematic spectral variations unequivocally confirm the successful incorporation of aliovalent ions and the resultant disruption of the spinel lattice symmetry[31]. Additionally, the supplementary Raman spectra show no discernible D or G bands, indicating that any carbonaceous residue is below the detection limit [Supplementary Figure 11]. This observation is fully consistent with the oxidative-annealing protocol used to obtain phase-pure oxides. X-ray photoelectron spectroscopy (XPS) was utilized to clarify the surface chemical states of the four specimens. Survey spectra, C 1s spectra, and O 1s spectra [Supplementary Figure 12] confirm the presence of Zn, Co, O, Fe, and Ni. High-resolution Co 2p spectra [Figure 3D] reveal a significant attenuation of the Co^{3+}-related signal in both $ZnCo_{2-y}Fe_yO_4$ and $Zn_{1-x}Co_{2-y}Ni_xFe_yO_4$ compared to pristine $ZnCo_2O_4$. This observation indicates the preferential substitution of Fe^{3+} at octahedral Co^{3+} sites, accompanied by a corresponding reduction in the surface content of Co^{3+}. The Fe 2p region [Figure 3E] is dominated by a Fe $2p_{3/2}$ peak at 710.8 eV[32], along with a satellite peak at 718.9 eV - features characteristic of Fe^{3+} - which corroborates the aforementioned substitution mechanism. The concurrent intensity attenuation of Zn $2p_{3/2}$ (1,021.8 eV, Figure 3F) suggests that Ni^{2+} preferentially substitutes Zn^{2+} located in the tetrahedral interstitial sites. In the high-resolution Ni 2p XPS spectrum [Figure 3G], the main peak centered at 855.7 eV and its corresponding shake-up satellite peak at 861.3 eV are in perfect agreement with the electronic configuration of Ni^{2+}. This further verifies that Ni is stably incorporated into the lattice with a +2 oxidation state. Finally, a comprehensive assessment of the porous architectures of the four as-synthesized materials was conducted using nitrogen physisorption integrated with Brunauer-Emmett-Teller (BET) analysis [Figure 3H and I, Supplementary Figure 13]. Among the series, the $Zn_{1-x}Co_{2-y}Ni_xFe_yO_4$ specimen demonstrated the most pronounced N_2 uptake capacity. Its adsorption-desorption isotherm conformed to a composite type IV/II profile[33], characterized by a distinct H3-type hysteresis loop-a feature indicative of a hierarchical pore network comprising both mesoporous and macroporous domains[34]. This intricate porous configuration exerts multiple synergistic effects that collectively enhance microwave-attenuation performance. Firstly, the high porosity inherently reduces the

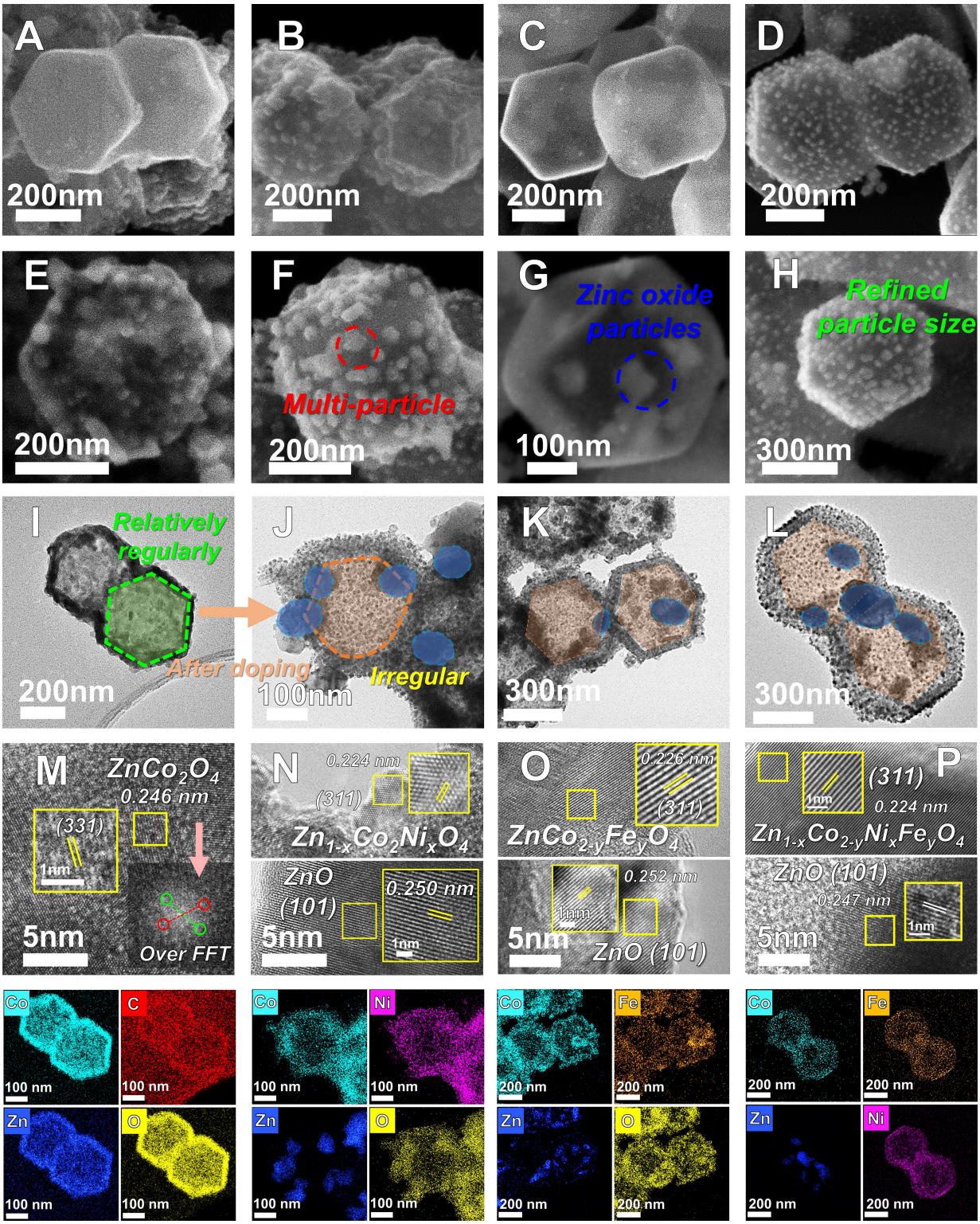

Figure 2. SEM, TEM, HRTEM and HAADF images of (A, E, I and M) $ZnCo_2O_4$, (B, F, J and N) $Zn_{1-x}Co_2Ni_xO_4$, (C, G, K and O) $ZnCo_{2-y}Fe_yO_4$ and (D, H, L and P) $Zn_{1-x}Co_{2-y}Ni_xFe_yO_4$. SEM: Scanning electron microscopy; TEM: transmission electron microscopy; HRTEM: high-resolution TEM; HAADF: high-angle annular dark field.

effective density of the absorber, a critical advantage for minimizing mass loading in practical applications where lightweight properties are paramount[35]. Secondly, the abundant heterointerfaces generated by the

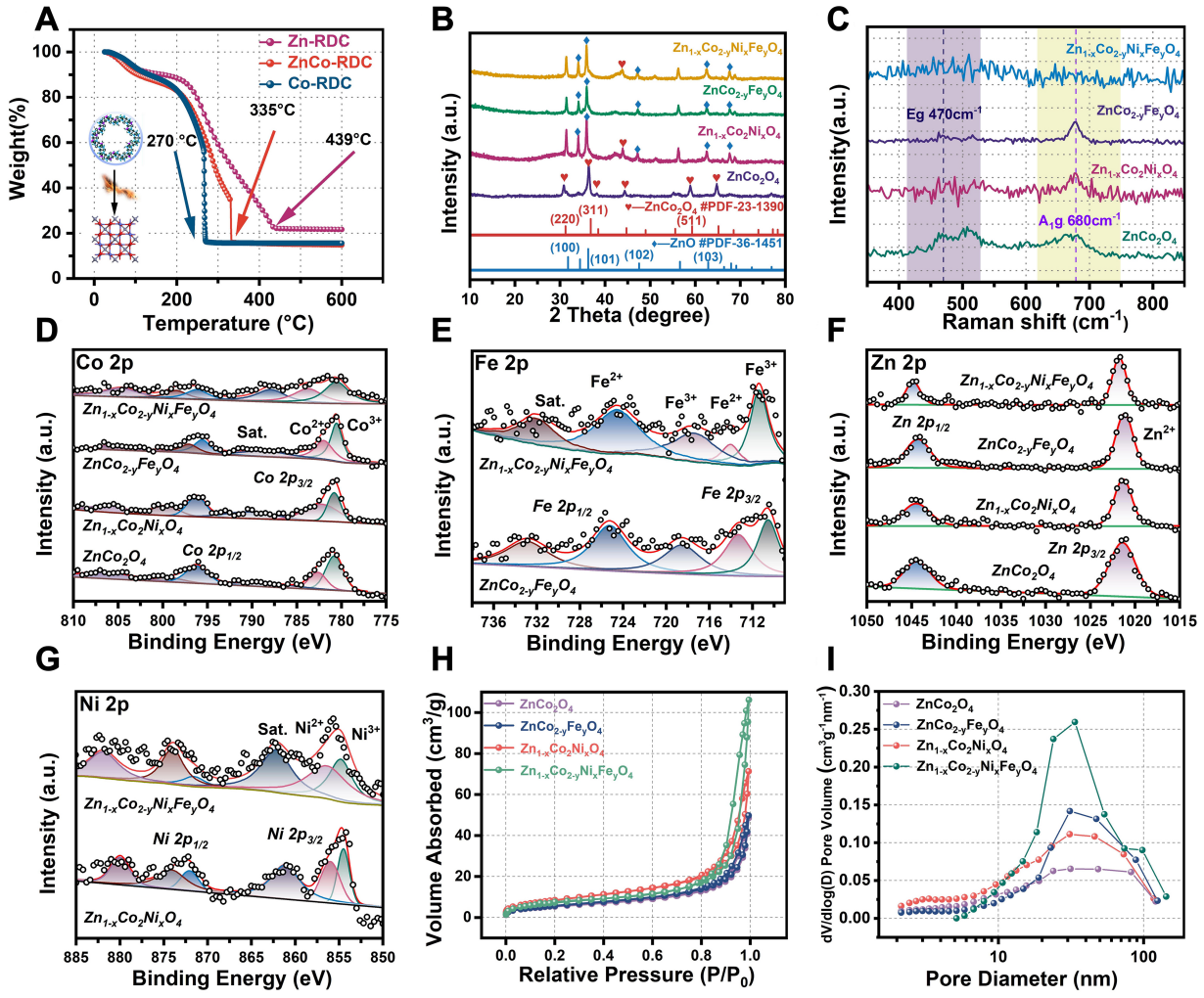

Figure 3. Characterization of $ZnCo_2O_4$, $Zn_{1-x}Co_2Ni_xO_4$, $ZnCo_{2-y}Fe_yO_4$ and $Zn_{1-x}Co_{2-y}Ni_xFe_yO_4$. (A) Thermogravimetric analysis (TGA) of ZnCo-RDC, Zn-RDC, and Co-RDC; (B) X-ray diffraction (XRD) patterns; (C) Raman spectra; (D) Co 2p X-ray photoelectron spectroscopy (XPS) spectra; (E) Fe 2p XPS spectra; (F) Zn 2p XPS spectra; (G) Ni 2p XPS spectra; (H) N_2 adsorption-desorption isotherms; (I) Pore-size distribution. RDC: Rhombic dodecahedral cage.

interconnected porous framework serve as extensive active sites for interfacial polarization (Maxwell-Wagner-Sillars effect), a key dielectric loss mechanism that significantly amplifies the dissipation of EM energy[36]. Notably, the BET-derived structural parameters-including specific surface area, total pore volume, and pore size distribution-exhibit excellent correlation with the EM performance data [reflection loss (RL) and EAB][37]. This consistency strongly corroborates that the graded porosity plays a pivotal role in optimizing microwave absorption, underscoring the importance of architectural engineering in conjunction with compositional regulation for developing high-performance EM wave absorbers.

Based on the transmission line theory, representative samples were selected for this study, with their RL performance evaluated under a constant filling ratio of 30 wt.% (detailed theoretical underpinnings are available in the Supplementary Materials). Experimental data derived from these measurements are presented separately in Figure 4 and Supplementary Figure 14. Compared with the oxides formed by the pyrolysis of solid ZIFs, hollow $ZnCo_2O_4$ [Figure 4A and B] exhibits both a moderate RL magnitude and a narrow EAB. However, the deliberate introduction of hierarchical porosity combined with ionic doping engineering generates a multitude of heterogeneous interfaces and lattice defects, thereby significantly enhancing EM wave attenuation[38]. For the Fe^{3+}-doped system $ZnCo_{2-y}Fe_yO_4$ [Figure 4C and D], the RLmin

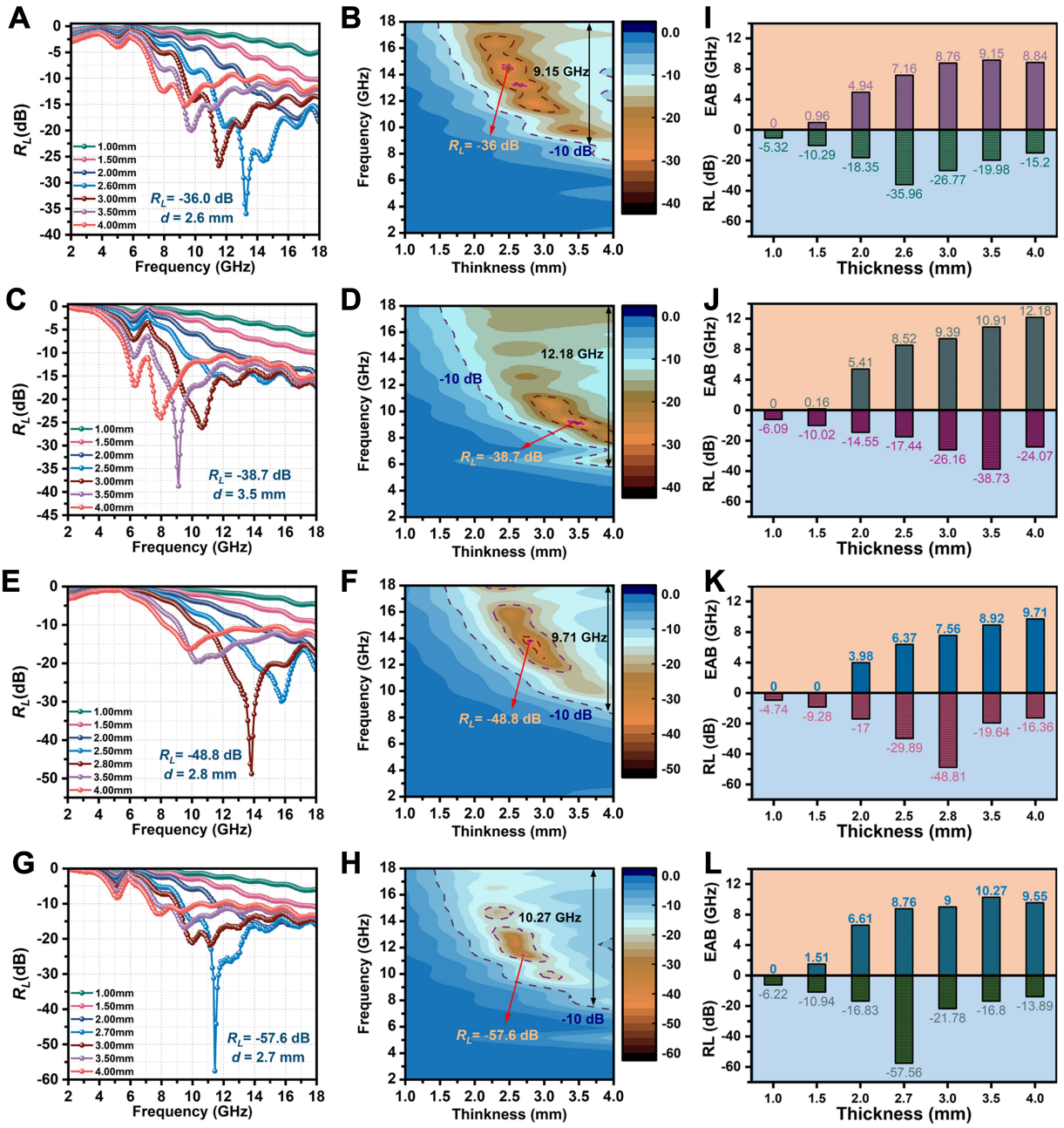

Figure 4. RL values and effective absorption bandwidths of (A, B and I) $ZnCo_2O_4$, (C, D and J) $ZnCo_{2-y}Fe_yO_4$, (E, F and K) $Zn_{1-x}Co_2Ni_xO_4$ and (G, H and L) $Zn_{1-x}Co_{2-y}Ni_xFe_yO_4$. RL: Reflection loss; EAB: effective absorption bandwidth.

reaches -38.7 dB, while the bandwidth corresponding to RL < -10 dB extends to 12.18 GHz. This confirms that Fe^{3+} incorporation effectively broadens the effective absorption window. In contrast, substitution with Ni^{2+} in $Zn_{1-x}Co_2Ni_xO_4$ [Figure 4E and F] drives the RLmin to -48.8 dB and yields an EAB of 9.71 GHz, demonstrating that Ni^{2+} doping is particularly effective in reducing the RLmin. Notably, co-doping with both metal ions in $Zn_{1-x}Co_{2-y}Ni_xFe_yO_4$ [Figure 4G and H] achieves a RLmin of -57.6 dB and an EAB of 10.27 GHz, simultaneously leveraging the advantages of each individual dopant. The thickness-dependent absorption performance of all four materials is visualized in the histograms of Figure 4I-L, facilitating an intuitive comparison. Progressive doping increases the structural complexity of the crystal lattice, and the dual-ion-doped composite successfully balances the ultralow RLmin characteristic of Ni^{2+} incorporation with the broad EAB associated with Fe^{3+} substitution[39]. Collectively, these findings demonstrate that the strategic integration of hierarchical porosity and judicious metal-ion doping represents a powerful approach to significantly enhancing EM wave absorption.

To experimentally validate the superiority of hollow architectures in enhancing EM absorption, the EM power-loss density of both solid and hollow configurations was numerically assessed using the finite-integration technique, with the results illustrated in Figure 5A. Compared to their solid counterparts, the hollow structures demonstrate a 195% enhancement in the spatially averaged electric field magnitude, accompanied by a striking 20.1% increase in the corresponding EM power dissipation. This substantial improvement can be attributed to the unique morphological features of the hollow architectures: the internal cavity enhances the interaction between the EM waves and the material's surface[40]. Additionally, the increased specific surface area of hollow structures provides more interfaces for interfacial polarization, thereby amplifying dielectric loss mechanisms[41]. These findings directly confirm that hollow architectures play a pivotal role in boosting EM wave attenuation, further supporting the design rationale of integrating structural engineering with compositional regulation for high-performance absorbers. The frequency-dependent real (ε′) and imaginary (ε″) components of the complex permittivity - along with the real (μ′) and imaginary (μ″) components of the complex permeability for the four specimens - are presented in Figure 5B-E. Upon doping, ε′ undergoes a significant upshift, which can be attributed to intensified ionic polarization and the proliferation of dipoles[42], collectively enhancing the overall polarization capacity. Among all compositions, the dual-ion-doped $Zn_{1-x}Co_{2-y}Ni_xFe_yO_4$ exhibits the highest average ε′, indicating its superior dielectric loss capability. Across the entire measured frequency band, ε′ of all samples shows a general decreasing trend[43]. Meanwhile, ε″ displays multiple resonance peaks arising from frequency dispersion and the activation of diverse polarization-relaxation mechanisms. Cole-Cole diagrams for the four materials are depicted in Supplementary Figure 15. The curves consist almost entirely of consecutive semicircles, confirming the coexistence of multiple polarization processes with distinct relaxation times[44]. Specifically, the heterointerface between ZnO and $ZnCo_2O_4$ induces a space-charge region due to carrier-concentration mismatch; this interfacial polarization relaxation, combined with bulk oxygen-vacancy polarization within ZnO, gives rise to the observed series of semicircles[45]. Furthermore, the progressive incorporation of metallic cations leads to a monotonic increase in both μ′ and μ″, indicating that ionic doping effectively enhances magnetic permeability and, consequently, improves overall microwave absorption performance. The overall dielectric and magnetic loss capabilities of the materials can be quantitatively evaluated using the dielectric loss tangent ($\tan\delta_\varepsilon = \varepsilon''/\varepsilon'$)[46] and the magnetic loss tangent ($\tan\delta_\mu = \mu''/\mu'$), respectively. As illustrated in Figure 5F, both $Zn_{1-x}Co_{2-y}Ni_xFe_yO_4$ and $ZnCo_{2-y}Fe_yO_4$ exhibit significantly higher $\tan\delta_\varepsilon$ values compared to pristine $ZnCo_2O_4$ or $Zn_{1-x}Co_2Ni_xO_4$. This observation confirms that the introduction of Fe^{3+} into the original spinel framework substantially enhances the dielectric loss capacity[47]. Regarding net magnetic loss, the trend aligns with that observed for μ′ and μ″: upon co-substitution of Co^{2+} and Fe^{3+}, the magnetic loss tangent increases markedly [Figure 5G]. Subsequently, the eddy current loss curve presented in Supplementary Figure 16 indicates that the magnetic loss mechanism arises from the synergistic superposition of ferromagnetic resonance and eddy current dissipation[48]. Magnetic hysteresis measurements [Supplementary Figure 17] reveal that the saturation magnetization (Ms) of $ZnCo_2O_4$ and $Zn_{1-x}Co_2Ni_xO_4$ is only 0.18 and 0.26 emu·g^{-1}, respectively - significantly lower than that of $ZnCo_{2-y}Fe_yO_4$ (5.5 emu·g^{-1}) and $Zn_{1-x}Co_{2-y}Ni_xFe_yO_4$ (7.71 emu·g^{-1}). The corresponding coercive fields (Hc) are 6.35, 61.62, 6.11, and 151.17 Oe, respectively. The pronounced enhancements in hysteresis loss induced by the incorporation of Fe^{3+} and Ni^{2+} further confirm that $Zn_{1-x}Co_{2-y}Ni_xFe_yO_4$ exhibits the largest magnetic loss tangent among all compositions[49]. Impedance matching represents another critical determinant of microwave absorption performance. The degree to which the magnitude of the normalized input impedance, $|Z_{in}/Z_0|$, approaches unity serves as a key indicator of optimal impedance matching between the absorber and free space[50]. Derived from the relative permittivity and permeability spectra, the $|Z_{in}/Z_0|$ curve of the dual-ion-doped composite $Zn_{1-x}Co_{2-y}Ni_xFe_yO_4$ closely approximates within the frequency band that overlaps with the RL < -10 dB region [Supplementary Figure 18], indicating efficient energy coupling between the material and incident EM waves. In contrast, the Fe-only-doped $ZnCo_{2-y}Fe_yO_4$ exhibits an impedance profile that deviates significantly from the ideal value, resulting in a pronounced mismatch[51]. Consequently, despite its inherently stronger EM dissipation capacity, $ZnCo_{2-y}Fe_yO_4$ demonstrates inferior absorption performance compared to $Zn_{1-x}Co_{2-y}Ni_xFe_yO_4$ due to

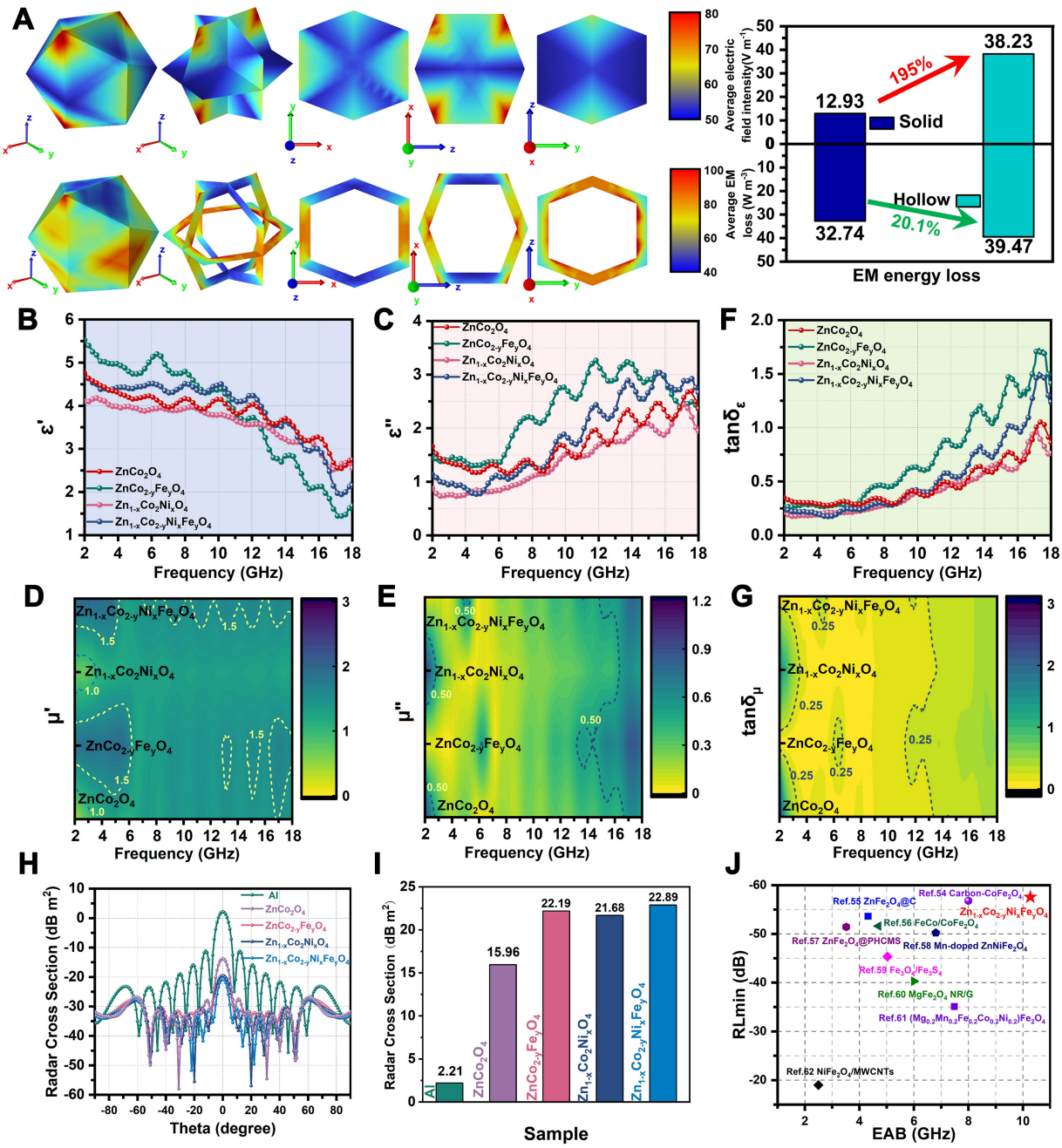

Figure 5. Electromagnetic absorption performance of $ZnCo_2O_4$, $Zn_{1-x}Co_2Ni_xO_4$, $ZnCo_{2-y}Fe_yO_4$ and $Zn_{1-x}Co_{2-y}Ni_xFe_yO_4$. (A) Simulated electromagnetic power loss density; (B and C) Real (ε′) and imaginary (ε″) parts of the relative permittivity; (D and E) Real (μ′) and imaginary (μ″) parts of the relative permeability; (F and G) Dielectric and magnetic loss tangents; (H and I) Radar cross-section (RCS) values; (J) Comparison of reflection loss (RL) and effective absorption bandwidth (EAB) of $Zn_{1-x}Co_{2-y}Ni_xFe_yO_4$ with previously reported absorbers[54-62]. EM: Electromagnetic.

inefficient wave coupling. The incorporation of bimetallic ions induces a significant number of lattice defects in $ZnCo_2O_4$, while simultaneously promoting the precipitation of zinc oxide particles. This results in the formation of abundant heterogeneous interfaces on the material surface, thereby enhancing EM wave absorption[52]. Furthermore, the material's unique hollow structure improves impedance matching and facilitates the penetration of EM waves, contributing to their efficient attenuation.

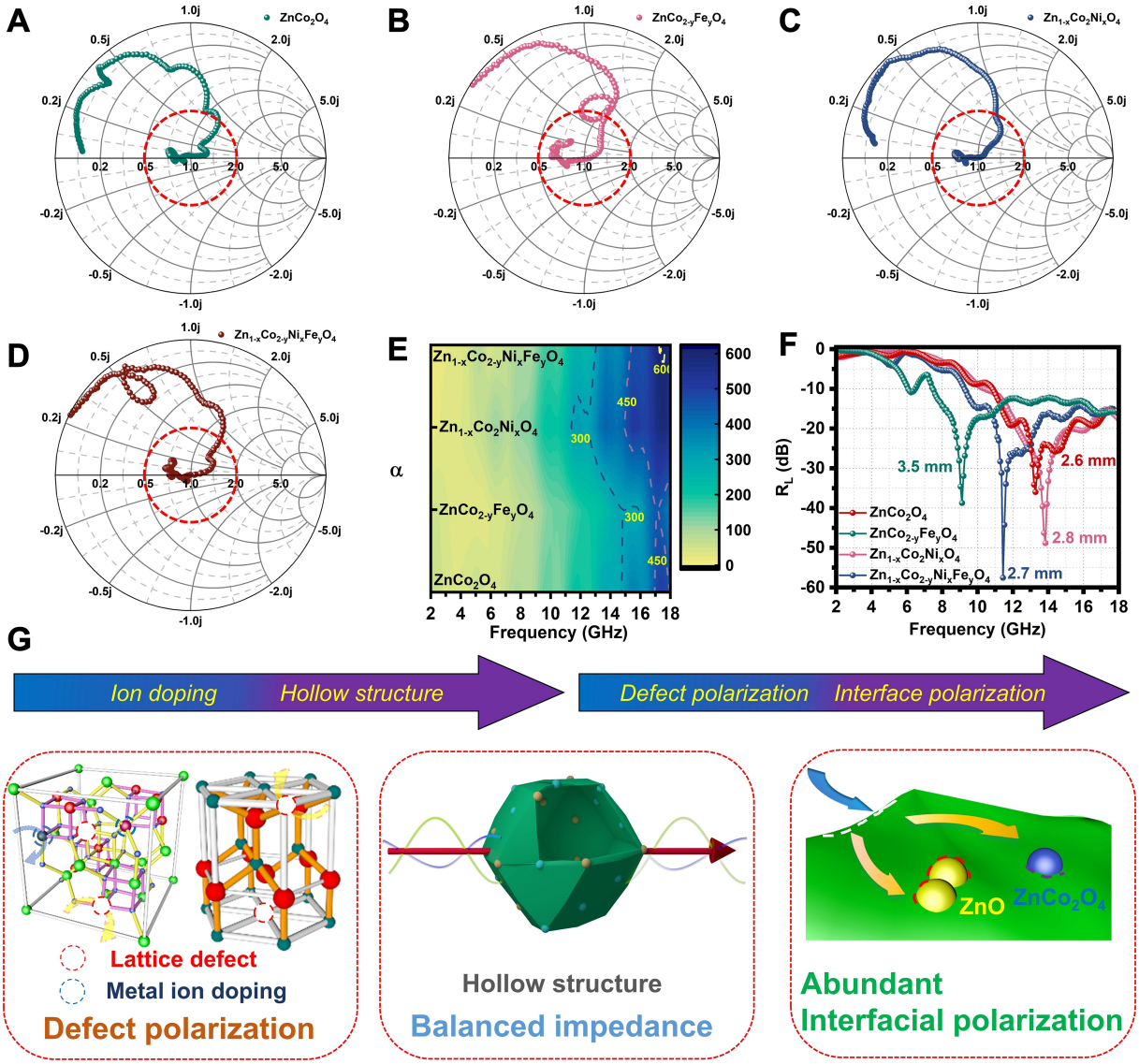

Figure 6. (A-D) Smith charts of $ZnCo_2O_4$, $Zn_{1-x}Co_2Ni_xO_4$, $ZnCo_{2-y}Fe_yO_4$ and $Zn_{1-x}Co_{2-y}Ni_xFe_yO_4$; (E) Attenuation constant (α) and (F) RLmin of the four absorbers; (G) Schematic illustration of the electromagnetic wave absorption mechanism of $Zn_{1-x}Co_{2-y}Ni_xFe_yO_4$. Panels (A-F) were plotted using Origin 2023. RLmin: Minimum reflection loss.

To further quantify the far-field performance of the four EM wave-absorbing materials, full-wave radar cross-section (RCS) simulations were performed using ANSYS HFSS (High Frequency Structure Simulator). In these simulations, each material was applied as a coating on a perfect electric conductor (PEC) slab. A 180 × 180 × 5 mm^3 aluminum plate was employed as the metallic substrate, with each absorber deposited at a mass fraction of 30%. The surrounding air domain was bounded by perfectly matched layers (PMLs) to minimize boundary reflections, and the coating thickness for each composite was set to its experimentally determined optimal matching thickness to ensure realistic performance evaluation. Figure 5H compares the monostatic RCS of the bare aluminum plate with that of the four coated configurations. It is evident that all absorber layers induce a significant RCS reduction relative to the uncoated reference[53]. Under normal incidence, the RCS values of the four coated specimens are notably lower than those of the bare plate. Quantitative comparisons are provided as bar charts in the inset of Figure 5I for clarity. Of particular note, the dual-ion-doped composite $Zn_{1-x}Co_{2-y}Ni_xFe_yO_4$ achieves an RCS reduction that is 43% greater than that of pristine $ZnCo_2O_4$, underscoring the synergistic benefits of its tailored composition and structure. Compared with analogous spinel-based EM wave-absorbing materials, the present composite exhibits superior EM

absorption performance [Figure 5J][54-62]. Collectively, the ultralow RLmin, broad EAB, superior impedance matching, and substantial RCS suppression exhibited by $Zn_{1-x}Co_{2-y}Ni_xFe_yO_4$ strongly validate its exceptional potential as a next-generation microwave-absorbing material, with promising implications for practical applications in radar stealth and EM pollution mitigation.

The Smith charts [Figure 6A-D] are used to assess the impedance-matching characteristics of the materials, where data points closer to the chart center indicate better impedance matching. Notably, $Zn_{1-x}Co_{2-y}Ni_xFe_yO_4$ shows a higher density of points near the center, demonstrating that the dual-ion-doped spinel structure exhibits superior impedance-matching performance[63]. To quantitatively assess the combined contributions of dielectric and magnetic losses to electromagnetic energy attenuation, the attenuation constant (α) was further evaluated[64]. Benefiting from its strong dielectric loss capability together with enhanced magnetic loss, $Zn_{1-x}Co_{2-y}Ni_xFe_yO_4$ exhibits the highest α value over the entire measured frequency range [Figure 6E]. This elevated attenuation constant directly accounts for its superior microwave absorption performance, confirming that the synergistic interplay between optimized impedance matching and efficient energy dissipation is essential for high-performance EM wave absorbers [Figure 6F and G].

CONCLUSIONS

In this work, we adopted a synergistic strategy combining the self-sacrificing template method and tannic acid-mediated multi-metal ion doping to synthesize hollow dodecahedral nanocages of $Zn_{1-x}Co_{2-y}Ni_xFe_yO_4$. The deliberate introduction of hetero-metal ions was found to induce lattice distortion and the exsolution of a secondary ZnO phase, thereby creating a high density of heterogeneous interfaces that significantly amplify interfacial polarization. Furthermore, the hollow architecture was strategically integrated to optimize impedance matching and reduce the effective density of the composite, ensuring superior attenuation performance. This integrated structural and compositional modulation paradigm is expected to facilitate the development of high-performance, lightweight microwave absorbers.

DECLARATIONS

Acknowledgments

The authors extend their gratitude to Ms. Zhang Yuyao (from Scientific Compass www.shiyanjia.com) for providing invaluable assistance with the BET analysis.

Authors' contributions

Writing-original draft preparation: Ding, L.; He, Z.
Writing-review and editing: Ding, L.; Zhang, R.; Liu, S.
Investigation: Geng, W.; Liu, P.
Supervision: Geng, W.; Liu, P.
Resources: Ding, L.; He, Z.; Zhang, R.; Liu, S.
Conceptualization: Liu, P.
Project administration: Liu, P.

Availability of data and materials

The data that support the findings of this study are available from the corresponding author upon reasonable request.

Financial support and sponsorship

This work was financially supported by the National Natural Science Foundation of China (52373271, 224751750) and Key Research and Development Project of Shaanxi Province (2025CY-YBXM-150).

Conflicts of interest

All authors declared that there are no conflicts of interest.

Ethical approval and consent to participate

Not applicable.

Consent for publication

Not applicable.

Copyright

REFERENCES

1. Wang, J.; Wang, B.; Wang, Z.; et al. Synthesis of 3D flower-like ZnO/$ZnCo_2O_4$ composites with the heterogeneous interface for excellent electromagnetic wave absorption properties. *J. Colloid. Interface. Sci.* **2021**, *586*, 479-90. DOI PubMed
2. Zhang, S.; Lan, D.; Zheng, J.; et al. Perspectives of nitrogen-doped carbons for electromagnetic wave absorption. *Carbon* **2024**, *221*, 118925. DOI
3. Liu, Y.; Tian, C.; Wang, F.; et al. Dual-pathway optimization on microwave absorption characteristics of core-shell Fe_3O_4@C microcapsules: composition regulation on magnetic core and MoS_2 nanosheets growth on carbon shell. *Chem. Eng. J.* **2023**, *461*, 141867. DOI
4. Qu, N.; Xu, G.; Liu, Y.; et al. Multi-scale design of metal-organic framework metamaterials for broad-band microwave absorption. *Adv. Funct. Mater.* **2025**, *35*, 2402923. DOI
5. Guo, Y.; Ruan, K.; Wang, G.; Gu, J. Advances and mechanisms in polymer composites toward thermal conduction and electromagnetic wave absorption. *Sci. Bull.* **2023**, *68*, 1195-212. DOI PubMed
6. Lv, H.; Yang, Z.; Pan, H.; Wu, R. Electromagnetic absorption materials: current progress and new frontiers. *Prog. Mater. Sci.* **2022**, *127*, 100946. DOI
7. Wu, Q.; Ma, Z.; Wang, C.; et al. Carbon nanofibers with small-sized Co nanoparticles and structural defects via a confined-coordination growth strategy toward electromagnetic wave absorption. *J. Adv. Ceram.* **2025**, *14*, 9221210. DOI
8. Huang, M.; Wang, L.; You, W.; Che, R. Single zinc atoms anchored on MOF-derived N-doped carbon shell cooperated with magnetic core as an ultrawideband microwave absorber. *Small* **2021**, *17*, e2101416. DOI PubMed
9. Lin, Y.; Zhou, X.; Wang, Y.; et al. Progress of MOFs composites in the field of microwave absorption. *Carbon* **2025**, *238*, 120241. DOI
10. Liu, A.; Xu, X.; Qiu, H.; et al. Bioinspired hollow heterostructure fillers for enhanced electromagnetic interference shielding in polyimide aerogels. *InfoMat* **2025**, *7*, e70060. DOI
11. Lou, Z.; Wang, Q.; Kara, U. I.; et al. Biomass-derived carbon heterostructures enable environmentally adaptive wideband electromagnetic wave absorbers. *Nano-Micro. Lett.* **2021**, *14*, 11. DOI PubMed PMC
12. Wen, B.; Cao, M.; Lu, M.; et al. Reduced graphene oxides: light-weight and high-efficiency electromagnetic interference shielding at elevated temperatures. *Adv. Mater.* **2014**, *26*, 3484-9. DOI PubMed
13. Xiao, J.; Zhan, B.; He, M.; et al. Interfacial polarization loss improvement induced by the hollow engineering of necklace-like PAN/carbon nanofibers for boosted microwave absorption. *Adv. Funct. Mater.* **2025**, *35*, 2316722. DOI
14. Zhao, T.; Jia, Z.; Zhang, Y.; Wu, G. Multiphase molybdenum carbide doped carbon hollow sphere engineering: the superiority of unique double-shell structure in microwave absorption. *Small* **2023**, *19*, e2206323. DOI PubMed
15. Gang, S.; He, H.; Long, H.; et al. 2D-high entropy alloys embedded in 3D-carbon foam towards light-weight electromagnetic wave absorption and hydrophobic thermal insulation. *Nano. Energy.* **2025**, *135*, 110642. DOI
16. Zhu, Y.; Liu, T.; Li, L.; Cao, M. Multifunctional WSe_2/Co_3C composite for efficient electromagnetic absorption, EMI shielding, and energy conversion. *Nano. Res.* **2024**, *17*, 1655-65. DOI
17. Liu, P.; He, Z.; Li, X.; Ding, L.; Liu, S.; Kong, J. Multifunctional hollow carbon microspheres enable superior electromagnetic wave response and corrosion barrier. *Adv. Mater.* **2025**, *37*, e2500646. DOI PubMed
18. Li, L.; Ban, Q.; Song, Y.; et al. Self-templating engineering of hollow N-doped carbon microspheres anchored with ternary FeCoNi alloys for low-frequency microwave absorption. *Small* **2024**, *20*, e2406602. DOI PubMed
19. Huang, H.; Wang, Y.; Yuan, S.; et al. Heteroatom-doped hollow bimetallic carbon nanofibers induce polarization-dominated multiple loss mechanisms for microwave absorption. *Chem. Eng. J.* **2025**, *507*, 160683. DOI
20. Shao, C.; Liu, H.; Shi, Y.; Tian, N.; You, C.; Zhao, Z. Dielectric-magnetic synergy in ferrite/carbon composites for electromagnetic microwave absorption. *Nano. Res.* **2025**, *18*, 94907815. DOI
21. Wu, Z.; Cheng, H. W.; Jin, C.; et al. Dimensional design and core-shell engineering of nanomaterials for electromagnetic wave absorption. *Adv. Mater.* **2022**, *34*, e2107538. DOI PubMed

22. Zhao, B.; Li, Y.; Zeng, Q.; et al. Galvanic replacement reaction involving core-shell magnetic chains and orientation-tunable microwave absorption properties. *Small* **2020**, *16*, e2003502. DOI PubMed
23. Chen, N.; Wang, R.; Pan, X.; et al. Hollow engineering of core-shell Fe_3O_4@MoS_2 microspheres with controllable interior toward optimized electromagnetic attenuation. *Adv. Compos. Hybrid. Mater.* **2025**, *8*, 1393. DOI
24. Ban, Q.; Li, L.; Liu, H.; et al. Polymerization-induced assembly-etching engineering to hollow Co@N-doped carbon microcages for superior electromagnetic wave absorption. *Carbon* **2023**, *215*, 118506. DOI
25. Liu, S.; Zhou, D.; Huang, F.; et al. Heterointerface engineering of polymer-based electromagnetic wave absorbing materials. *Soft. Sci.* **2025**, *5*, 7. DOI
26. Ma, Z.; Yang, K.; Li, D.; et al. The electron migration polarization boosting electromagnetic wave absorption based on Ce atoms modulated yolk@shell Fe_xN@NGC. *Adv. Mater.* **2024**, *36*, e2314233. DOI PubMed
27. Lian, Y.; Han, B.; Liu, D.; et al. Solvent-free synthesis of ultrafine tungsten carbide nanoparticles-decorated carbon nanosheets for microwave absorption. *Nano-Micro. Lett.* **2020**, *12*, 153. DOI PubMed PMC
28. Zhou, X.; Jia, Z.; Zhang, X.; et al. Electromagnetic wave absorption performance of $NiCo_2X_4$ (X = O, S, Se, Te) spinel structures. *Chem. Eng. J.* **2021**, *420*, 129907. DOI
29. Wu, P.; Wang, J.; Li, J.; Feng, J.; He, W.; Guo, H. Pseudo-binary composite of Sr_2TiMoO_6-Al_2O_3 as a novel microwave absorbing material. *Rare. Met.* **2025**, *44*, 503-14. DOI
30. Zhu, S.; Shu, J.; Cao, M. Tailorable MOF architectures for high-efficiency electromagnetic functions. *Mater. Chem. Front.* **2021**, *5*, 6444-60. DOI
31. Zhang, Y.; Zhu, C.; Gao, S. Multi-scale magnetic and electric interaction in gradient magnetic-dielectric heterostructures with excellent low-frequency electromagnetic wave absorption. *Nano. Res.* **2025**, *18*, 94907622. DOI
32. Zhao, Z.; Zhang, L.; Wu, H. Hydro/organo/ionogels: “controllable” electromagnetic wave absorbers. *Adv. Mater.* **2022**, *34*, e2205376. DOI PubMed
33. Zhao, Y.; Wang, W.; Wang, Q.; et al. Construction of excellent electromagnetic wave absorber from multi-heterostructure materials derived from $ZnCo_2O_4$ and ZIF-67 composite. *Carbon* **2021**, *185*, 514-25. DOI
34. Li, T.; Ma, L.; Wang, L.; et al. Ultra-wide band electromagnetic wave absorption by decorating the magnetic particles on two-dimensional $Ti_3C_2T_x$. *Rare. Met.* **2025**, *44*, 1844-55. DOI
35. Qi, J.; Liang, C.; Ruan, K.; et al. Cactus-like architecture for synergistic microwave absorption and thermal management. *Natl. Sci. Rev.* **2025**, *12*, nwaf394. DOI PubMed PMC
36. Zhao, H.; Xu, X.; Wang, Y.; et al. Heterogeneous interface induced the formation of hierarchically hollow carbon microcubes against electromagnetic pollution. *Small* **2020**, *16*, e2003407. DOI PubMed
37. Zhan, B.; Qu, Y.; Qi, X.; et al. Mixed-dimensional assembly strategy to construct reduced graphene oxide/carbon foams heterostructures for microwave absorption, anti-corrosion and thermal insulation. *Nanomicro. Lett.* **2024**, *16*, 221. DOI PubMed PMC
38. Su, X.; Wang, J.; Liu, T.; et al. Controllable atomic migration in microstructures and defects for electromagnetic wave absorption enhancement. *Adv. Funct. Mater.* **2024**, *34*, 2403397. DOI
39. Nguyen, T. T.; Edalati, K. High-entropy oxide with tailored heterogeneous electronic structure as a low-bandgap catalyst for antibiotic photodegradation under visible light. *Appl. Catal. B:. Environ. Energy.* **2026**, *382*, 126011. DOI
40. Wang, Y.; Zhao, P.; Liang, B.; Chen, K.; Wang, G. Carbon nanotubes decorated Co/C from ZIF-67/melamine as high efficient microwave absorbing material. *Carbon* **2023**, *202*, 66-75. DOI
41. Guo, S.; Zhu, J.; Song, Z.; et al. Multispectral $ErBO_3$@ATO porous composite microspheres with laser and electromagnetic wave compatible absorption. *Rare. Met.* **2023**, *42*, 2406-18. DOI
42. Sun, R.; Lv, H.; Lian, G.; et al. Dielectric shell regulation in synergy FeCoNi@$ZnIn_2S_4$ microspheres with broadband electromagnetic wave absorption. *Soft. Sci.* **2025**, 5. DOI
43. Zhang, Y.; Kong, J.; Gu, J. New generation electromagnetic materials: harvesting instead of dissipation solo. *Sci. Bull.* **2022**, *67*, 1413-5. DOI PubMed
44. Wang, X.; Pan, F.; Xiang, Z.; et al. Magnetic vortex core-shell Fe_3O_4@C nanorings with enhanced microwave absorption performance. *Carbon* **2020**, *157*, 130-9. DOI
45. Hai, H. T. N.; Arita, M.; Edalati, K. High-entropy perovskites as new photocatalysts for cocatalyst-free water splitting. *Appl. Catal. B:. Environ. Energy.* **2026**, *383*, 126081. DOI
46. Lv, H.; Cui, J.; Li, B.; Yuan, M.; Liu, J.; Che, R. Insights into civilian electromagnetic absorption materials: challenges and innovative solutions. *Adv. Funct. Mater.* **2025**, *35*, 2315722. DOI
47. Ren, S.; Yu, H.; Wang, L.; et al. State of the art and prospects in metal-organic framework-derived microwave absorption materials. *Nano-Micro. Lett.* **2022**, *14*, 68. DOI PubMed PMC

48. Ma, D.; Zhang, Y.; Gao, S. Magnetic-dielectric synergy in manganese ferrite/coal gasification fine slag composites for broadband electromagnetic wave absorption. *Chem. Eng. Sci.* **2026**, *320*, 122480. DOI
49. Wang, N.; Kou, X.; Zhong, L.; et al. Geometry-defect-spin coupling in chiral high-entropy systems: multiscale mechanisms of GHz electromagnetic dissipation. *Sci. Adv.* **2025**, *11*, eadz2218. DOI PubMed PMC
50. Xiong, T.; Luo, Y.; Qian, Y.; et al. High electromagnetic wave absorption and flame retardancy performance from NF@HCS/NF-filled epoxy-based electronic packaging material. *J. Mater. Chem. A.* **2024**, *12*, 1094-105. DOI
51. Hidalgo-jiménez, J.; Akbay, T.; Sauvage, X.; Ishihara, T.; Edalati, K. Mixed atomic-scale electronic configuration as a strategy to avoid cocatalyst utilization in photocatalysis by high-entropy oxides. *Acta. Materialia.* **2025**, *283*, 120559. DOI
52. Li, Y.; Xiong, T.; Xu, C.; et al. Al_2O_3/h-BN/epoxy based electronic packaging material with high thermal conductivity and flame retardancy. *J. Appl. Polym. Sci.* **2023**, *140*, e53291. DOI
53. Zhao, Y.; Wang, N.; Wang, H.; et al. Chiral structure induces spatial spiral arrangement of Fe_3O_4 nanoparticles to optimize electromagnetic wave dissipation. *Appl. Phys. Lett.* **2024**, *124*, 161901. DOI
54. Cao, R.; Qiu, Y.; Zhao, X.; et al. Carbon-$CoFe_2O_4$ composite with hierarchical porous structure for efficient microwave absorption. *Diamond. Relat. Mater.* **2025**, *157*, 112542. DOI
55. Jiang, J.; Lan, D.; Li, Y.; et al. Construction of spherical heterogeneous interface on $ZnFe_2O_4$@C composite nanofibers for highly efficient microwave absorption. *Ceram. Int.* **2024**, *50*, 38331-41. DOI
56. Liu, M.; Zhao, B.; Pei, K.; et al. An ion-engineering strategy to design hollow FeCo/$CoFe_2O_4$ microspheres for high-performance microwave absorption. *Small* **2023**, *19*, e2300363. DOI
57. Chai, L.; Wang, Y.; Zhou, N.; et al. *In-situ* growth of core-shell $ZnFe_2O_4$ @ porous hollow carbon microspheres as an efficient microwave absorber. *J. Colloid. Interface. Sci.* **2021**, *581*, 475-84. DOI PubMed
58. Mandal, D.; Bhandari, B.; Mullurkara, S. V.; Ohodnicki, P. R. All-around electromagnetic wave absorber based on Ni-Zn ferrite. *ACS. Appl. Mater. Interfaces.* **2024**, *16*, 33846-54. DOI PubMed PMC
59. Wu, H.; Liu, J.; Liang, H.; Zang, D. Sandwich-like Fe_3O_4/Fe_3S_4 composites for electromagnetic wave absorption. *Chem. Eng. J.* **2020**, *393*, 124743. DOI
60. Chen, W.; Liu, Q.; Zhu, X.; Fu, M. One-step *in situ* growth of magnesium ferrite nanorods on graphene and their microwave-absorbing properties. *Appl. Organomet. Chem.* **2018**, *32*, e4017. DOI
61. Ma, J.; Zhao, B.; Xiang, H.; et al. High-entropy spinel ferrites MFe_2O_4 (M = Mg, Mn, Fe, Co, Ni, Cu, Zn) with tunable electromagnetic properties and strong microwave absorption. *J. Adv. Ceram.* **2022**, *11*, 754-68. DOI
62. Guo, L.; He, Y.; Chen, D.; et al. Hydrothermal synthesis and microwave absorption properties of nickel ferrite/multiwalled carbon nanotubes composites. *Coatings* **2021**, *11*, 534. DOI
63. Xiang, X.; Gao, S.; Zhang, Y. Magnetic-electric synergistic coal gangue-based high-efficiency electromagnetic wave absorber. *Chem. Eng. J.* **2025**, *524*, 169310. DOI
64. Qian, Y.; Gang, S.; Li, Y.; et al. Advanced multifunctional IGBT packing materials with enhanced thermal conductivity and electromagnetic wave absorption properties. *J. Colloid. Interface. Sci.* **2024**, *653*, 617-26. DOI PubMed